Geophysical Journal International

Geophys. J. Int. (2019) **219,** 1032–1042
Advance Access publication 2019 July 26
GJI Seismology

doi: 10.1093/gji/ggz345

Spurious low velocity zones in joint inversions of surface waves and receiver functions

Chao Gao, Erin Cunningham and Vedran Lekić

Department of Geology, University of Maryland, College Park, MD, USA. E-mail: cgao1@terpmail.umd.edu

Accepted 2019 July 25. Received 2019 July 18; in original form 2019 June 19

SUMMARY

Low-velocity layers within the crust can indicate the presence of melt and lithologic differences with implications for crustal composition and formation. Seismic wave conversions and reverberations across the base of the crust or intracrustal discontinuities, analysed using the receiver function method, can be used to constrain crustal layering. This is commonly accomplished by inverting receiver functions jointly with surface wave dispersion. Recently, the proliferation of model-space search approaches has made this technique a workhorse of crustal seismology. We show that reverberations from shallow layers such as sedimentary basins produce spurious low-velocity zones when inverted for crustal structure with surface wave data of insufficiently high frequency. Therefore, reports of such layers in the literature based on inversions using receiver function data should be re-evaluated. We demonstrate that a simple resonance-removal filter can suppress these effects and yield reliable estimates of crustal structure, and advocate for its use in receiver-function based inversions.

Key words: Crustal structure; Inverse theory; Surface waves and free oscillations.

1 INTRODUCTION

Constraints on the layering and seismic velocities of Earth's continental crust provide key insights on its composition and formation (e.g. Christensen & Mooney 1995; Rudnick & Fountain 1995). However, accurate quantification of crustal velocity structures from seismological observations is challenging, with primary constraints often coming from active-source experiments (for a recent review, see Mooney 2015). Recently, passive source seismic investigations of continental crust structure have benefited from the installation of massive seismic arrays (e.g. USArray Transportable Array; Superior Province Rifting Earthscope Experiment [Zhang *et al.* 2016]) and the development in improved imaging techniques (Shapiro *et al.* 2005; Kumar & Bostock 2008; Langston & Liang 2008; Rychert & Harmon 2016).

Consequently, efforts at combining different seismic observables to improve the constraints on crustal models have grown. Among those, joint inversions of surface wave dispersion (SWD) and receiver functions (RFs, Özalaybey *et al.* 1997; Julia *et al.* 2000; Tkalčić *et al.* 2006; Bodin *et al.* 2012; Shen *et al.* 2013; Chai *et al.* 2015) have gained in popularity due to their complementary constraints: absolute seismic velocities from SWD and sharp impedance contrasts from RFs. The resulting crustal models revealed features in greater detail and with smaller uncertainties, including sharp discontinuities in the lithospheric mantle (Bodin *et al.* 2016; Calo *et al.* 2016) and crustal low velocity zones in various tectonic settings (Ward *et al.* 2014; Li *et al.* 2017; Li *et al.* 2018).

While the complementarity of SWD and RF sensitivity helps reduce the non-uniqueness of the seismic inverse problem (e.g. Özalaybey *et al.* 1997), differences in their inherent resolving power can introduce inconsistencies between the two data types (e.g. Chai *et al.* 2015). The consequences of these inconsistencies on the inversion results have not been adequately quantified, especially across diverse geological settings. Additional complications arise in regions where the low-velocity sedimentary layers overlay crystalline continental crust; the strong impedance contrast at the bottom of the sediment layer can produce high amplitude, long duration reverberations in the RFs that could bias estimates of crustal thickness (Yeck *et al.* 2013; Yu *et al.* 2015).

In this study, we assess the potential for artifacts in joint seismic inversions for crustal structure using a novel implementation of transdimensional Bayesian (TB) inversion of SWD and RFs measured across 49 stations of the EarthScope Transportable Array. We focus on the Trans-Hudson Orogen and Superior Craton, part of which is overlain by the Williston Basin. We compare our results with analyses using synthetic data and discuss approaches for mitigating these effects.

2 DATA AND METHOD

2.1 Ps receiver functions from transportable array

We focus on the east side of the Williston Basin where the thickness of the sedimentary layer varies from 0 to 5 km (see Fig. 1a) from

Downloaded from https://academic.oup.com/gji/article-abstract/219/2/1032/5539534 by University of Maryland user on 03 September 2019

© The Author(s) 2019. Published by Oxford University Press on behalf of The Royal Astronomical Society.

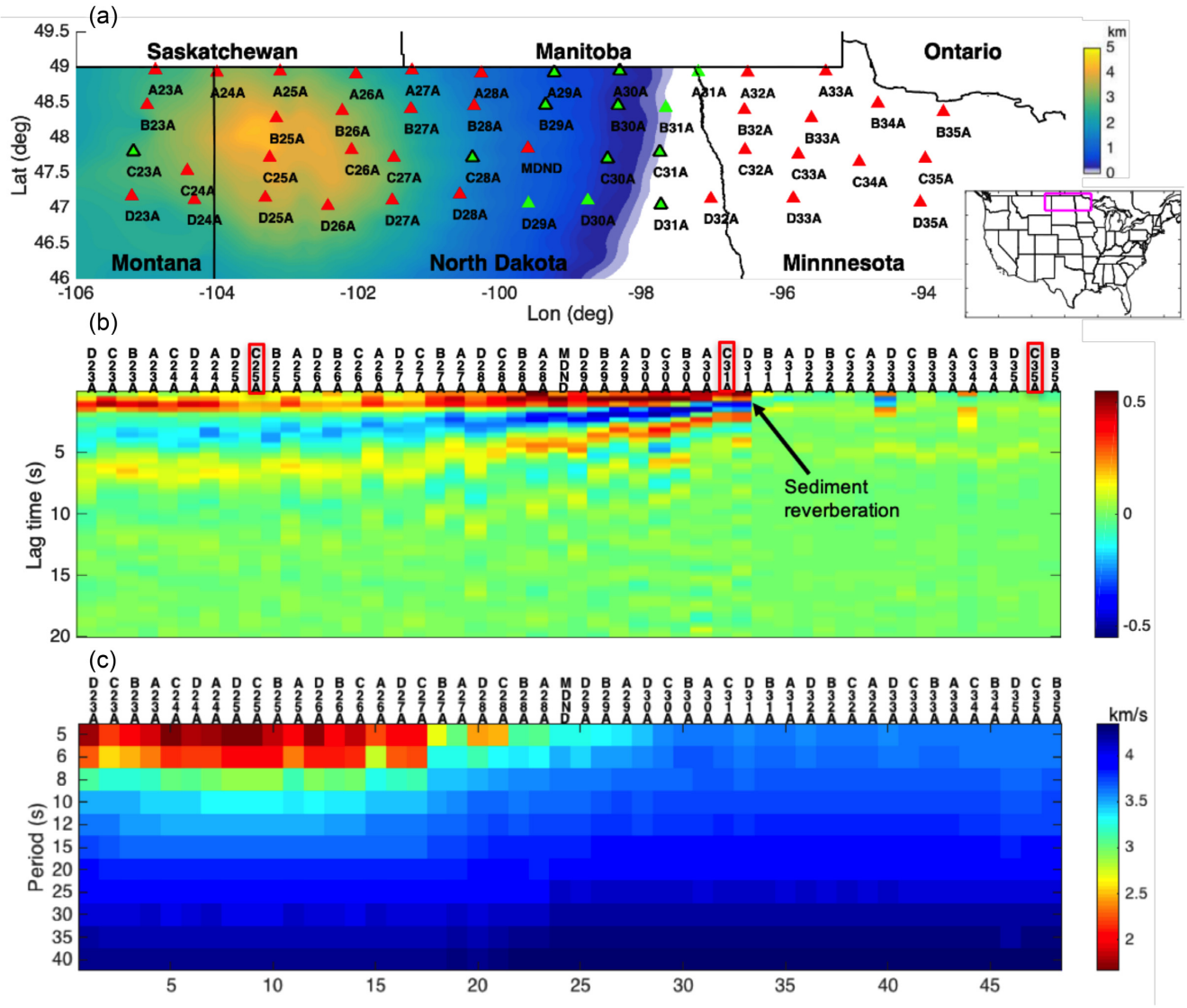

Figure 1. (a) Sediment thickness (Marshak *et al.* 2017) across the study area (magenta box in inset); Transportable Array (TA) stations (triangles). Red triangles show the stations where sediment correction is not needed, green triangles show the stations where the sediment correction are applied in order to retrieve reliable posterior. The green triangles with black contour are the stations where spurious low velocity zones are resolved when sediment correction is not applied to RFs for the joint inversion. (b) Ps RFs and (c) Love wave phase velocities at the TA stations shown in (a), sorted by longitude from west to east. Three stations are highlighted in (b) as they will be discussed in detail in the paper.

east to west (e.g. Nelson *et al.* 1993; Marshak *et al.* 2017), and utilize data from EarthScope Transportable Array.

At each station, we compute P-to-s receiver functions using 300 s three-component waveforms around the *P* arrival time from $M_w > 5.5$ events at 30–90° epicentral distance, which are transformed into the *P*–SV system using the free-surface transform matrix (Kennett 1991). Optimal free-surface velocities are obtained by minimizing the SV energy on the *P* component at the time of the *P* arrival, and are listed in Table S1. It has been shown that RFs in P–SV–SH system yield superior constraints on subsurface structure compared to *Z*–*R* receiver functions (Reading *et al.* 2003). We follow the Abt *et al.* (2010) procedure and cull the data set to include data with a minimum *Z*-to-*R* cross correlation of 0.3, and a maximum 25 s discrepancy between the automatically determined arrival time and prediction for ak135. We window the *P* and SV waveforms prior to deconvolution and apply a fourth order Butterworth bandpass filter to waveforms of 0.03–1 Hz. We then use the iterative time domain deconvolution with Gaussian half-amplitude half-width of ∼0.5 s to calculate the receiver functions (Ligorria & Ammon 1999).

These data selection criteria yield between 76 and 338 RFs at each station, which we divide into 2–6 equal-sized bins based on their ray parameters to explicitly account for ray-parameter dependence of RF waveforms. In each RF bin, we apply bootstrap sampling to compute the average Ps RF and estimate its uncertainty. Figs S1–S3 show the individual Ps RFs as well as binned-average Ps RFs for the three stations on which we focus our discussion in this paper. In these figures, individual RFs are coloured according to their ray-parameter bin to illustrate that the binning by ray parameter allows us to account for potential amplitude variations within the RF. Due to the limited deployment time (18–24 months) of the Transportable Array, RF analyses using TA data generally suffer from incomplete backazimuthal coverage. In this study, we plot the RFs with respect to backazimuth to make sure they do not exhibit strong signs of

Downloaded from https://academic.oup.com/gji/article-abstract/219/2/1032/5539534 by University of Maryland user on 03 September 2019

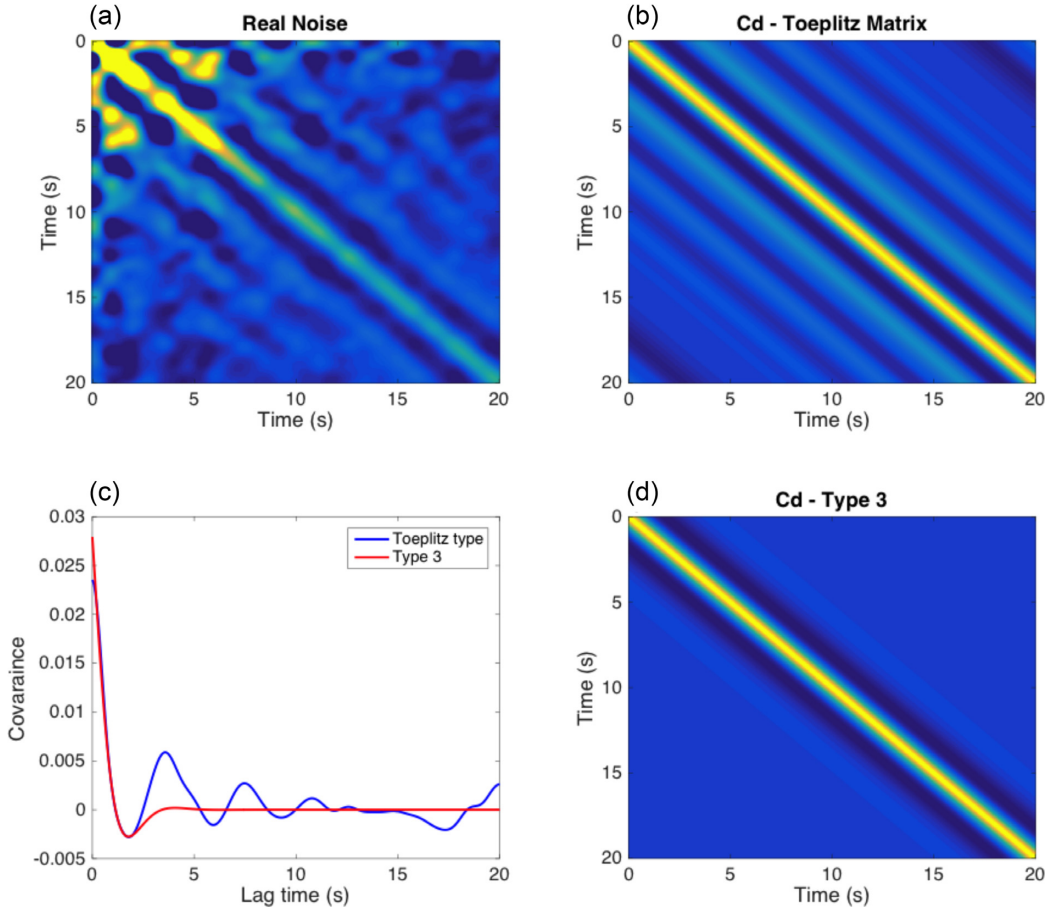

Figure 2. Noise characterization of receiver functions. Top left-hand panel: data covariance matrix estimated from 338 Ps receiver functions calculated at station MDND-TA. Top right-hand panel: a Toeplitz-type data covariance matrix constructed from the average covariance as a function of lag-time determined from the data covariance matrix in the top left. Bottom left-hand panel: data covariance from Toeplitz type data covariance matrix versus type 3 parametrization proposed by Kolb & Lekic (2014) as a function of lag time. Bottom right-hand panel: covariance matrix corresponding to best-fitting type 3 parametrization to the average covariance as a function of lag-time.

azimuthal anisotropy (Figs S1–S3). Since we already binned the receiver functions based on their ray-parameter, the limited number of events available for the Transportable Array does not enable us to further divide the data set by backazimuth to account for anisotropy while maintaining robustness of the RF estimates.

The average Ps RFs for each station are arranged by longitude and shown in Fig. 1(b). Strong reverberations at the beginning of the Ps RFs are observed to the west, suggesting a layer on top of the crust bounded by large impedance contrast; such signal is not seen to the east. Both features are consistent with the trend of basement depth from Marshak *et al.* (2017). To quantify uncertainty of binned RFs, we could use RFs within bins as samples for estimating the data covariance matrix (C_D). However, the relatively small number of samples available for this computation reduces its reliability, and yields singular and ill-conditioned C_D (e.g. Ledoit & Wolf 2004). Instead, we represent C_D with three parameters (Kolb & Lekic 2014) obtained by minimizing the L_1 norm to the average covariance versus lag time estimated across RFs (see Fig. 2). At each station, a data covariance matrix is estimated following the procedure illustrated in Fig. 2. This is done to capture potential variations in noise characteristics across different locations.

2.2 Surface wave dispersion from transportable array

At the station coordinates, we also extract Rayleigh and Love wave dispersion curves between 5 and 40 s period from the transdimensional hierarchical Bayesian (THB) phase velocity maps (Olugboji *et al.* 2017) based on ambient noise measurements of Ekström (2017). The THB approach used to create the phase velocity maps yields ensembles of solutions, enabling uncertainties to be quantified. Fig. 1(c) shows the Love wave dispersion data projected onto the TA stations in the study area; the dispersion curves arranged by station longitude reflect the trends of the sedimentary thickness map, confirming that sediment thickness variations manifest clearly in the SWD data. However, unlike the Ps RF data, SWD data on the edge of the Williston basin do not bear the signature of the sediment layer even at the shortest period measured (see B29A—D31A from Figs 1b and c). This difference will be further discussed in the results section.

2.3 TB joint inversion with a progressive inclusion scheme

Joint inversions of SWD and RFs are highly non-linear and non-unique (e.g. Ammon *et al.* 1990). Though linearized inversions

Downloaded from https://academic.oup.com/gji/article-abstract/219/2/1032/5539534 by University of Maryland user on 03 September 2019

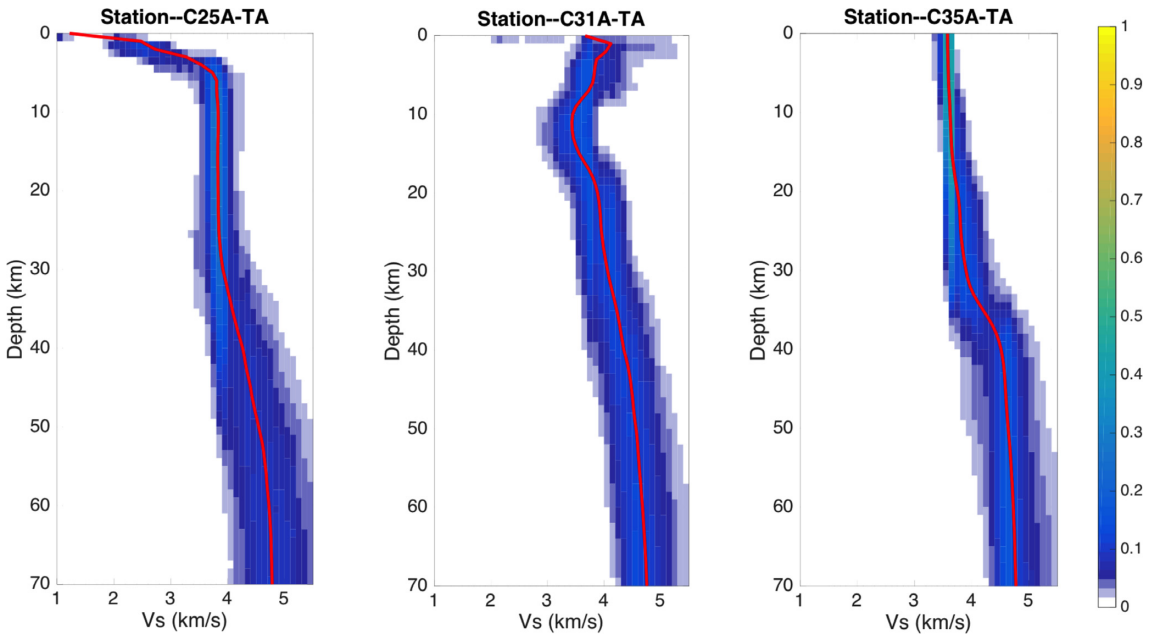

Figure 3. V_s depth distributions from transdimensional Bayesian inversion of surface wave dispersion and Ps RFs for stations C25A-TA (left-hand panel), C31A-TA (middle panel), C35A-TA (right-hand panel). The ensemble solutions are displayed as probability density functions at each depth, with warmer colours corresponding to higher posterior probabilities, and the solid red line denoting the 5 per cent trimmed mean of the posterior. NB: The low-velocity layer between 8 and 17 km at C31A is likely an artefact (see discussion in Section 4).

have been performed in the past (Owens *et al.* 1984; Kosarev *et al.* 1993), they are easily trapped by local minima, making the final model strongly dependent on the starting model. Furthermore, linearized inversions often seek a single model that minimizes the misfit function and approximate uncertainty of the model parameters in ways that may not adequately represent the full uncertainty. Here, we opt for a Bayesian inversion using a model space sampling framework that embraces the non-linearity and non-uniqueness of seismic inversion. Seismic Bayesian joint inversions of SWD and RFs with fixed parametrizations (Shen *et al.* 2013; Shen & Ritzwoller 2016) have been used to retrieve an ensemble of lithospheric shear velocity structures compatible with the data, enabling uncertainty quantification on a data set of continental scale. To allow a more flexible parametrization that introduces less prior information, a transdimensional sampling method was proposed and applied to the joint inversion of SWD and RFs (Piana Agostinetti & Malinverno 2010; Bodin *et al.* 2012). Unlike most of the seismic inverse problems, transdimensional inversions treat the number of model parameters as an unknown. It has been shown that the posterior distribution acquired through TB inversions is naturally parsimonious (Malinverno 2002) due to the Bayesian formulation of model selection (Malinverno 2000; Sivia & Skilling 2006). This property of TB inversions punishes more complicated models and therefore restricts the inverse problem from overfitting the data. Instead, TB inversions produce an ensemble solution where the model complexity is primarily determined by the data itself.

Implementations of TB inversions of SWD and RFs have previously been described in the literature (e.g. Bodin *et al.* 2012). We adopt a similar approach by applying a reversible jump Markov chain Monte Carlo (rj-McMC) algorithm, but differ from Bodin *et al.* (2012) in some respects: (1) we explicitly use covariance matrices representing data uncertainty, ensuring optimal information extraction from the two data types; (2) we do not impose fixed V_p–V_s and density–V_s scaling relationships based on prior knowledge, because inverting for V_p/V_s and density along with V_s minimizes potential bias (Dettmer *et al.* 2015; Kim *et al.* 2016; Gao & Lekic 2018). We assign uniform distributions between 0.5 and 5.5 km s^{-1}, 1.6–1.9 and 2.6–3.1 g cm^{-3} for V_s, V_p/V_s and density, respectively and (3) we implement a progressive inclusion scheme for the RF data, which is described below.

A major challenge for probabilistic sampling approaches is achieving convergence quickly and efficiently exploring the model space, especially when involving multimodal density functions such as those associated with RF inversion. We use a progressive-inclusion scheme to optimize convergence. We start by inverting SWD data for 5×10^5 iterations using the approach of Gao & Lekic (2018), who found that convergence is approached in around 10^5 iterations regardless of starting model. Using the latter 2.5×10^5 steps, we construct an estimate of a velocity structure that we then use as a starting model for the joint inversion of SWD and RF data. The joint inversion also proceeds in a progressive fashion, initially including the first 3 s of the Ps RFs to compute the likelihood using the Mahalanobis distance (for 1×10^5 iterations), before proceeding to include the first 5 s for additional 1×10^5 iterations, and finally inverting the 15-s-long Ps RFs for additional 3×10^5 iterations to complete the inversion. 1×10^4 samples are drawn from this final chain to create the ensemble solution, which can be used to compute the uncertainty on the V_p and V_s inferences. During final segment of the progressive inclusion, we ensure the misfit remains low and stable along the iteration after the burn-in period. Additionally, we verify that the statistical properties of the models do not change between the first and second half of the ensemble. Finally, we also show the comparison of the model prediction from the posterior and the observation (right-hand panel of Figs S4–S6) to assess the convergence of the rj-McMC.

Downloaded from https://academic.oup.com/gji/article-abstract/219/2/1032/5539534 by University of Maryland user on 03 September 2019

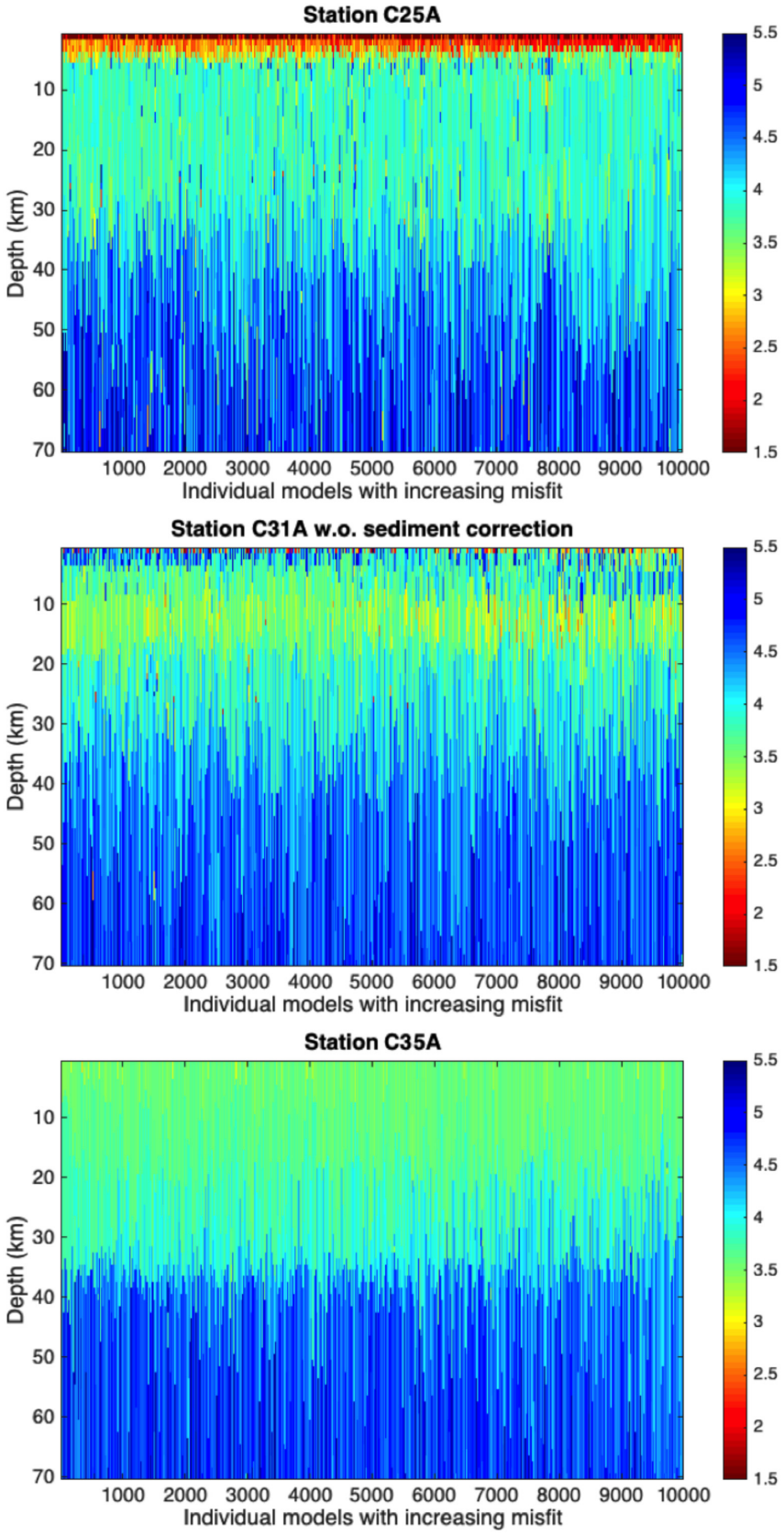

Figure 4. Individual 1-D velocity models from the ensemble solution of C25A, C31A and C35A joint inversion (Fig. 3) sorted by their misfit in an ascending order.

Downloaded from https://academic.oup.com/gji/article-abstract/219/2/1032/5539534 by University of Maryland user on 03 September 2019

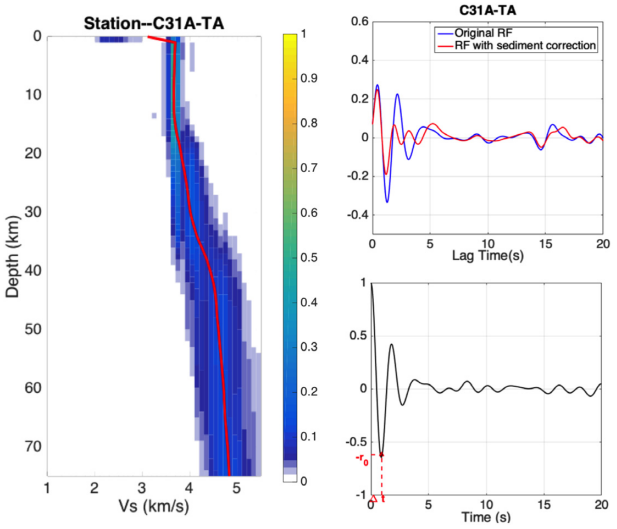

Figure 5. Left-hand panel: V_s depth distributions from TB inversion of SWD and resonance-removed Ps RF data at station C31A-TA. The ensemble solutions and the 5 per cent trimmed mean of the posterior (red) are shown as in Fig. 2. Right top-hand panel: comparison of RFs before (blue) and after (red) applying the resonance removal filter. Right bottom-hand panel: autocorrelation of original RF showing how Δt and r_0 are measured.

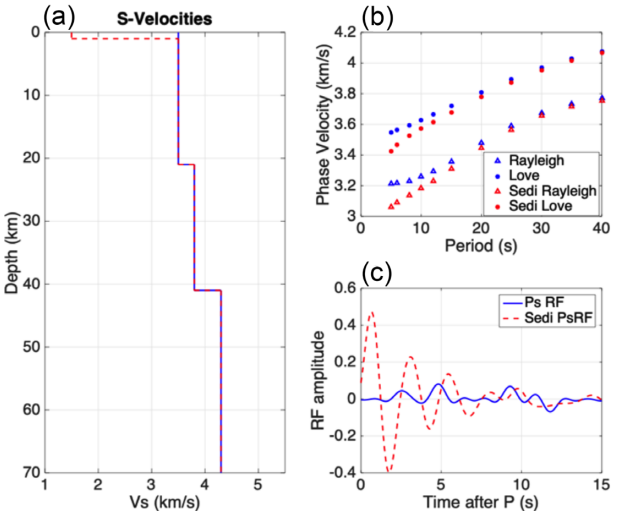

Figure 6. (a) 1-D synthetic V_s model with (red) and without (blue) a sedimentary layer. (b) Associated Rayleigh and Love phase velocities and (c) Ps RFs from the model with (red) and without (blue) a sedimentary layer.

3 RESULTS

3.1 *Joint Inversion of SWD and Ps RFs*

We perform a TB joint inversion of SWD and Ps RFs at three TA stations within the study area, selected as archetypes of different scenarios controlled by the thickness of the sedimentary layer (Fig. 3). The sedimentary layer thicknesses for C25A, C31A and C35A are approximately 4, 1 and 0 km, respectively (Marshak *et al.* 2017). Though we invert for structure down to 100 km depth, here we only present the top 70 km in order to highlight the crustal structure. To aid in the identification of layering in the ensemble models, we

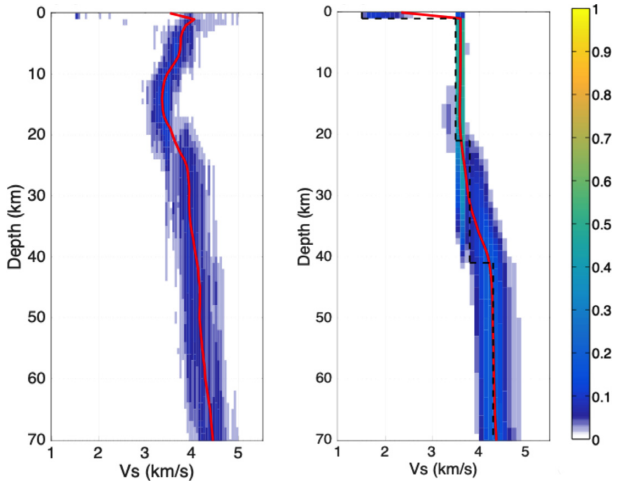

Figure 7. Left-hand panel: V_s depth distributions from TB inversion of synthetic SWD and Ps RF data. SWD data are generated for model without a sedimentary layer, while the Ps RF data are generated for the model with a sedimentary layer (black dashed lines). The ensemble solutions are displayed as probability density functions at each depth, and the solid red line denoting the 5 per cent trimmed mean of the posterior. Right-hand panel: Same as the left-hand panel, except that the resonance removal filter has been applied to the Ps RF.

compute and plot the probability of a V_s change—called a transition probability—at every 1 km depth (see Figs S4–S6).

The posterior distributions of V_s retrieved from the joint inversion are intriguing. For station C35A, we see a 36 km thick, two-layer crustal structure. According to the transition probability, the most abrupt V_s jump within the crust occurs around 20 km. The average shear velocity above 20 km is 3.62 km s^{-1}, while the average shear velocity between 21 and 36 km is 3.86 km s^{-1}. No sedimentary layer is resolved at this location. The SWD and RF predicted by the ensemble solution reasonably fit the observations (Figs S4–S6), confirming that the models are consistent with the data.

Unlike C35A, both C25A and C31A resolve a thin, low velocity layer at shallowest depths, which we interpret as the sedimentary layer. The posterior distribution of V_s at C25A resolves two layers within the 2.9-km-thick sediment package (see Fig. S7 for a zoomed in version): the top layer has an average V_s of 1.12 km s^{-1} and a thickness of 0.8 km; the bottom layer has an average shear velocity of 2.47 km s^{-1} and a thickness of 2.1 km. No clear crustal layering is resolved for this station; the Moho is resolved as a relatively gradual V_s increase between the 35 and 50 km, where the trimmed mean of V_s changes from 3.8 to 4.6 km s^{-1}. The V_s structure retrieved from C31A station shows a one-layer, 0.8-km-thick sedimentary layer (see Fig. S7). Based on the estimate of trimmed mean, the shear velocity changes drastically from 1.90 to 3.74 km s^{-1} right below the sedimentary layer. While the crust beneath C31A appears to be relatively fast in V_s in the upper crust, V_s drops significantly at around 8 km depth to 3.57 km s^{-1} , and an intracrustal LVZ appears to span the 8–17 km depth range. To demonstrate that such LVZ feature is not due to the choice of the summary statistics of the trimmed mean, we analyse the posterior distribution obtained by the Bayesian inversion, which is shown in Fig. S7. A multimodal velocity distribution below the C31A sediment layer is observed across the ensemble, demonstrating the non-uniqueness of the inversion due to lack of data constraints. The posterior distribution of C31A between the depth of 5 and 15 km appears to be non-Gaussian, with a switch

Downloaded from https://academic.oup.com/gji/article-abstract/219/2/1032/5539534 by University of Maryland user on 03 September 2019

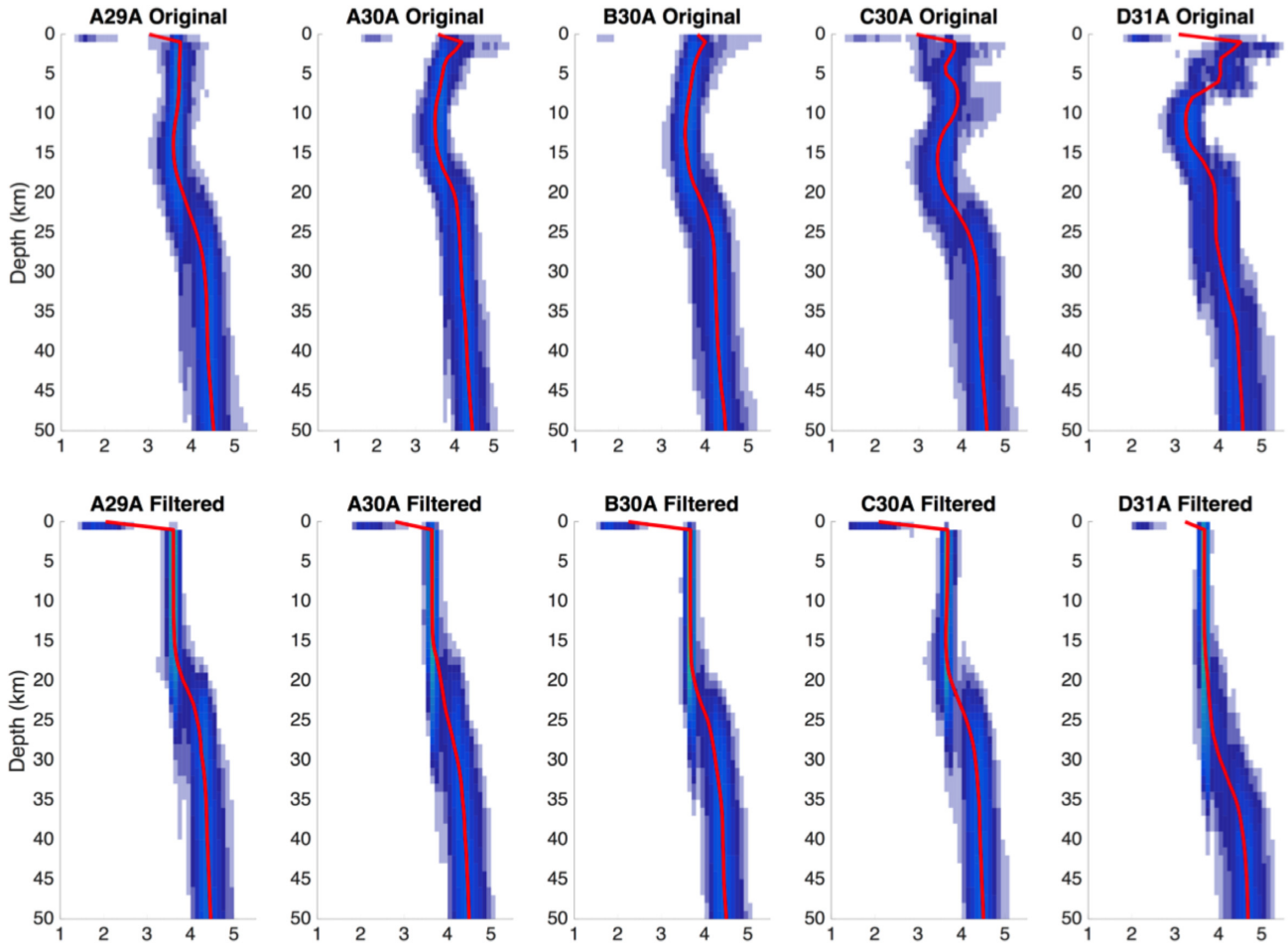

Figure 8. Posterior distributions from joint inversion with SWD and original RFs (upper panel) and from joint inversion with SWD and sediment-corrected RFs (lower panel) for five selected stations.

of skewness from positive to negative around 8 km. In contrast, the posterior at the same depth for C25A is more Gaussian-like with a tighter variation, suggesting a relatively well-constrained velocity structure. In Fig. 4, we show the individual models from the ensemble solution—representing samples from the posterior—sorted by their fit to the data in an ascending order. This arrangement makes it very clear not only that a significant portion of the posterior bears a clear LVZ signature in the mid-crust of C31A, but that LVZs are more prominent on the left, meaning that models with LVZ are preferred by the data. The Moho depth is inferred at 40 km. For both C25A and C31A, the SWD and RF predicted by these structures agree well with observations (Figs S4 and S5).

3.2 *Joint Inversion of SWD and Ps RFs, correcting for sediment layer*

The significant impedance contrast between the sedimentary layer and the underlying crystalline crust can produce large amplitude reverberations that appear as a decaying, oscillatory signal in RFs. These shallow layer reverberations can overprint signals from direct conversions across the Moho and other intra- and subcrustal interfaces, making it difficult to resolve accurate crustal structure (Zelt & Ellis 1999). Yu *et al.* (2015) proposed an approach to effectively remove such near surface reverberation by applying a resonance removal filter. To assess the significance of these reverberations to joint SWD and RF inversion for crustal structure, we use this filter to obtain resonance-removed RFs that we invert jointly with SWD data using our TB approach.

To construct the resonance removal filter, the traveltime of the *S* reverberation in sediment, Δt, and the relative strength of the Ss reverberation, r_0 are needed. The effect of the reverberation removal filter on the RFs can be dramatic. Fig. 5 shows a comparison between the original mean RF and the mean resonance-removed RF for station C31A. It can be seen that the potential sediment reverberation right after the direct sediment conversion has been significantly reduced after applying the filter, clarifying signals from later lag-times, corresponding to greater depths.

After computing the resonance removal filter for each station, we repeat our joint TB inversion using the resonance-removed RFs but introduce a fixed one-layered 'sediment' at the top of the model. Since the traveltime of the *S* reverberation in sediment, Δt, is used to construct the removal filter, our fixed 'sediment' layer needs to have the correct combination of thickness and V_s to be consistent with the Δt. During the inversion, we first propose a V_s value for the 'sediment' layer, V_{s_0} and then calculate the thickness, H, using the equation:

$$H = (\Delta t/2)\sqrt{V_{s_0}^{-2} - p^2},$$

Downloaded from https://academic.oup.com/gji/article-abstract/219/2/1032/5539534 by University of Maryland user on 03 September 2019

where p stands for the median ray parameter of the binned receiver function. At each step of the rj-McMC chain, we introduce a 1-in-5 chance of perturbing V_{s_0} in the range of 0–V_{s_1} km s^{-1}; where V_{s_1} is the shear velocity value of the layer right beneath the fixed 'sediment' layer. This allows H to vary during the inversion while remaining consistent with the resonance removal filter.

The V_s posterior distribution of the inversion is show in Fig. 5. The retrieved sedimentary layer has a thickness of 1 km and an average V_s of 2 km s^{-1}, which is similar as the sedimentary layer resolved in the inversion with original RFs. The most prominent difference between the two inversion results is the crustal structure. In this inversion, no crustal LVZ is resolved; the trimmed mean of V_s increases from 3.59 to 4.04 km s^{-1} along the depth, with one abrupt V_s jump around 18 km. The Moho depth is inferred at 37 km.

Apart from the inversion with station C31A, we also perform TBI with SWD and resonance-removed RFs for C25A, where the rj-McMC struggles to converge. Given the same number of iterations, the retrieved ensemble for C25A (Fig. S8) resolves multiple sharp V_s drops within a small depth range. Meanwhile, the predicted RFs and Love wave dispersion at 5, 6 s from the ensemble fits poor with the observation, suggesting the inversion is unable to converge, especially for the shallow structure.

4 DISCUSSION

The TB inversion results from the three selected stations show intriguing and contrasting effects of sediment on the retrieval of structure. The three selected seismic stations are located in the Superior Craton and Trans-Hudson Orogen (Whitmeyer & Karlstrom 2007). Crustal LVZs are not expected in this region, and active source seismological studies find no evidence for them (Nelson *et al.* 1993). At C35A, where no sediment layer is present, the TB inversion resolves a seismic structure where the V_s increases with depth. In that case, our implementation of rj-McMC with a progressive inclusion scheme enables a fast, stable convergence. The shear velocity structure is well constrained in terms of both absolute value and sharp changes such as crustal layering and Moho.

At station C31A, lying on 1 km of sediment, we resolve the sedimentary layer in both inversions, whether using the original RFs or the resonance-removed RFs. However, the inversion using the original RFs also contains an unexpected LVZ in the mid-crust; no LVZ is present in the inversion of RFs where sedimentary reverberations have been removed. We interpret the LVZ retrieved as an artifact resulting from the non-uniqueness of inverting RFs containing large amplitude oscillatory reverberations together with SWD measurements that lack constraints on the sedimentary layer, either because it is too thin for the period range of SWD or because it is a local feature not resolved in the construction of the phase velocity maps. Another possibility is that although both RFs and SWD contain sufficient constraints at the topmost depth, they introduce conflicting information leading to the spurious LVZ. To rule out this possibility, we conduct a TB joint inversion with the SWD starting from 15 to 40 s and uncorrected RFs (Fig. S9). In this way, we further reduce the strength of SWD at shallow depths. The retrieved ensemble still resolves a crustal LVZ, consistent with the interpretation that the presence of LVZ is not due to the conflicting constraints but is instead due to lack of constrains on absolute V_s. This implies that crustal velocity structure should be carefully examined when SWD measurements in short period are unavailable, or when only RFs are used.

We confirm the paucity of SWD constraint on the sediment at C31A, by performing a TB inversion using only SWD. The retrieved V_s structure (Fig. S10) does not resolve any low-velocity layer on top of the crust, strongly suggesting that the SWD data do not see a low-velocity layer. Meanwhile, the RF data show large amplitude oscillations at early lag times (Fig. 5), indicating the existence of a large impedance contrast at shallow depths. When only the Ps RF is used in the TB inversion (Fig. S11), the retrieved V_s structure resolves as spurious mid-crustal low-velocity layer, as expected. We stress that absolute velocities are not well constrained in the RF only inversion due to lack of data sensitivity. Once we apply the resonance removal filter, the signals after the first peak are significantly reduced, confirming that the signal comes from the sediment reverberation, rather than from abrupt, intracrustal V_s drops. Therefore, in joint inversions of SWD and uncorrected RFs, constraints on V_s in the shallowest few kilometres only come from the first few seconds of the RFs, which, on their own, only very weakly constrain V_s (e.g. Bodin *et al.* 2012). However, since this part of the RFs is dominated by both the direct conversion and sedimentary multiples, the joint inversion readily obtains structures with redundant sharp velocity changes due to the lack to constraints on absolute V_s .

To further investigate the origin of the intracrustal LVZs, we carry out synthetic tests that reproduce them and illustrate why applying resonance removal to the RFs helps prevent their appearance. Fig. 6(a) shows two simple velocity models constructed to allow differences in predicted SWD and RFs to be straightforwardly attributed to the presence of a sediment layer. One model (red) has 1 km of sediment (V_s = 1.5 km s^{-1}), on top of a two-layer crust with a Moho depth of 41 km. The V_s is 4.3 km s^{-1} below the Moho. The second model is identical to the first, except that it lacks a sediment layer. Differences in predicted SWD due to the sediment are limited to only the shortest periods (Fig. 6b); given that typical measurement uncertainties in this period range are $\sim$0.1 km s^{-1}, they would be difficult to detect in realistic data. However, the differences between RFs due to the sediment are much more prominent; S wave reverberations within the sediment produce large amplitude oscillations that overprint the direct Moho conversion.

In order to recreate a scenario where SWD measurement is incapable of constraining the sediment layer, we perform joint TB inversion using calculated SWD data from the model without sediment together with the RFs from the model with sediment. The retrieved V_s structure (Fig. 7left-hand panel) resolves a mid-crustal LVZ that does not exist in either synthetic model. After applying a reverberation removal filter to the RFs and repeating the inversion, the LVZ no longer appears in the retrieved V_s structure (Fig. 7 right-hand panel).

One might argue that the spurious LVZ results from using SWD predicted from a model without a sediment layer. We agree that given sufficiently accurate and precise SWD measurements, the appearance of the spurious LVZ could be mitigated as illustrated in a synthetic test in Fig. S12. However, the situation illustrated by our synthetic test is common in practice mainly due to the way SWD is measured. Unlike RFs, which are single-station-based observables, SWD curves are extracted from phase velocity maps whose resolution is imperfect due to data coverage and modelling assumptions. Therefore, while RF data are sensitive to the subsurface structure directly beneath the seismic station, surface wave dispersion curves might not be, particularly when dealing with structures of limited spatial extent and/or data from less dense seismic deployments.

Previously, Chai *et al.* (2015) suggested that this potential discrepancy in sensitivity between RFs and SWD should be addressed

Downloaded from https://academic.oup.com/gji/article-abstract/219/2/1032/5539534 by University of Maryland user on 03 September 2019

by spatially smoothing the RFs to make their resolution more comparable to that of SWD maps. Here, we show that this degradation of RF data is not always needed. By applying a resonance-removal filter to our RFs, we are able to reduce the non-uniqueness of the inverse problem. Additionally, by requiring the two-way traveltime of *S* wave in the sediment (Δt) to fit the value estimated from the autocorrelation of the RFs, we pose a stronger prior constraint on the TB inversion to help better constrain the sediment structure. However, crustal V_s structures constrained from RFs only or RFs together with long period SWD data should be interpreted with extreme caution due the possibility of crustal artifacts.

The joint inversion with SWD and resonance-removed RFs for station C25A does not converge in our tests. As is suggested by Yu *et al.* (2015), the resonance removal filter may perform poorly when the sediment layer is too thick due to several reasons: the rapid decay of reverberations with time; weak impedance contrast at the bottom of the sediment layer that is unable to generate significant reverberations; or complexity within the sediment layer requiring more accurate modelling of the reverberations. At C25A, we believe that the complex sediment structure is the main reason for the failed convergence of the joint inversion. During the inversion, the resonance removal filter that is applied to all proposed RFs assumes a single-layer sediment, which is unlikely. On the contrary, the inversion with SWD and original RFs resolved a more realistic shear velocity structure, with no crustal artifacts. Unlike station C31A, the SWD data used for station C25A show a strong low velocity signal at shallow depths. Our inversion with only SWD for C25A confirms this observation (Fig. S13), the retrieved V_S structure resolves a clear low-velocity sediment layer. We believe that the strong signal of the sediment layer in the SWD data, as well as the relatively low measurement error associated with them, helps better constrain the shallow part of the structure beneath C25A even without applying the resonance removal filter. Therefore, due to better constraints from SWD and the unsuitability of a single-layer resonance removal filter we advise that inversions use SWD and the original RFs in locations where the thick sediment layers are expected. In Fig. 8, we show comparisons between the joint inversion of original RFs and of the sediment-corrected RFs for five additional seismic stations within our study area. Crustal LVZs are observed at all five stations, and are effectively removed by the sediment-correction. We want to point out that although it is clear that the sediment removal filter is suitable for the thin, single-layer sediment setting, sediment thickness should not be used as the sole criterion to determine whether or not to apply a sediment correction. Both the layering and the frequency range of available SWD data should also be considered. Because information about sediment layering and basin complexity is typically limited, it is seldom useful to rely on a measure of sedimentary basin complexity for guidance on whether or not to apply the sediment removal filter. Cunningham and Lekic (in revision at GJI) proposed approaches for evaluating the effectiveness of the sediment removal filter by comparing the change of RF waveform as well as the fit of the RF autocorrelation to a decaying sinusoid. In Fig. 1(a), we highlighted the seismic stations where the sediment removal filter is needed to retrieve accurate velocity structures using green colour.

We also want to point out that applying a sediment resonance removal filter does not prohibit the retrieval of a real crustal LVZ. In Fig. S14, we show a synthetic test where a mid-crust LVZ is imposed in the true model. By performing TB joint inversion of SWD and sediment-corrected Ps RFs, the posterior is able to resolve the LVZ without significantly losing constraints on other features of the true model, such as the sediment layer and Moho.

5 CONCLUSIONS

In this paper, we investigated the reliability of crustal structure inferences using an implementation of TB method capable of simultaneously inverting surface wave dispersion and receiver functions. We documented that shallow sedimentary layers can produce spurious intracrustal LVZs in joint seismic inversions and proposed an approach for removing these artifacts. We found that in locations where surface wave data and RFs show consistent signal of the shallowest layers—no sediment is expected by both data types or the sedimentary layer is sufficiently thick to be seen by both data types—TB joint inversions are able to retrieve realistic crustal structures. Finally, we showed that applying a sediment resonance removal filter to our RFs can effectively remove the sediment reverberation, enabling recovery of a more realistic crustal model without LVZs.

Seismological studies have identified crustal LVZs in various geological settings (Kind *et al.* 1996; Beck & Zandt 2002; Zorin *et al.* 2002; Li *et al.* 2003). While most such LVZs are reported in active orogens, some studies have suggested their presence in cratonic regions (Chen *et al.* 2015). Our results indicate that the inferences of LVZs from joint inversions should be scrutinized in sedimented regions. Furthermore, they provide guidance on best practices for avoiding spurious intracrustal LVZs and performing reliable joint inversion of SWD and RFs under different shallow-layer scenarios.

ACKNOWLEDGEMENTS

The authors thank Lara S. Wagner for extensive suggestions that have improved this manuscript. We also thank the editor Lapo Boschi and two anonymous reviewers for their constructive reviews. We acknowledge support from NSF grants EAR 1352214 and EAR 1361325, as well as the Packard Fellowship for Science and Technology to VL.

REFERENCES

Abt, D.L., Fischer, K.M., French, S.W., Ford, H.A., Yuan, H. & Romanowicz, B., 2010. North American lithospheric discontinuity structure imaged by Ps and Sp receiver functions, *J. geophys. Res.: Solid Earth,* **115**(B9).

Ammon, C.J., Randall, G.E. & Zandt, G., 1990. On the nonuniqueness of receiver function inversions, *J. geophys. Res.: Solid Earth,* **95**(B10), 15303–15318.

Beck, S.L. & Zandt, G., 2002. The nature of orogenic crust in the central Andes, *J. geophys. Res.: Solid Earth,* **107**(B10).

Bodin, T., Leiva, J., Romanowicz, B., Maupin, V. & Yuan, H., 2016. Imaging anisotropic layering with Bayesian inversion of multiple data types, *Geophys. J. Int.,* **206**(1), 605–629.

Bodin, T., Sambridge, M., Tkalčić, H., Arroucau, P., Gallagher, K. & Rawlinson, N., 2012. Transdimensional inversion of receiver functions and surface wave dispersion, *J. geophys. Res.: Solid Earth,* **117**(B2).

Calò, M., Bodin, T. & Romanowicz, B., 2016. Layered structure in the upper mantle across North America from joint inversion of long and short period seismic data, *Earth planet. Sci. Lett.,* **449,** 164–175.

Chai, C., Ammon, C.J., Maceira, M. & Herrmann, R.B., 2015. Inverting interpolated receiver functions with surface wave dispersion and gravity: application to the western US and adjacent Canada and Mexico, *Geophys. Res. Lett.,* **42**(11), 4359–4366.

Chen, Y., Gu, Y.J., Dokht, R.M. & Sacchi, M.D., 2015. Crustal imprints of Precambrian orogenesis in western Laurentia, *J. geophys. Res.: Solid Earth,* **120**(10), 6993–7012.

Christensen, N.I. & Mooney, W.D., 1995. Seismic velocity structure and composition of the continental crust: a global view, *J. geophys. Res.: Solid Earth,* **100**(B6), 9761–9788.

Downloaded from https://academic.oup.com/gji/article-abstract/219/2/1032/5539534 by University of Maryland user on 03 September 2019

Dettmer, J., Dosso, S.E., Bodin, T., Stipčević, J. & Cummins, P.R., 2015. Direct-seismogram inversion for receiver-side structure with uncertain source–time functions, *Geophys. J. Int.,* **203**(2), 1373–1387.

Ekström, G., 2017. Short-period surface-wave phase velocities across the conterminous United States, *Phys. Earth planet. Inter.,* **270,** 168–175.

Gao, C. & Lekić, V., 2018. Consequences of parametrization choices in surface wave inversion: insights from transdimensional Bayesian methods, *Geophys. J. Int.,* **215**(2), 1037–1063.

Julia, J., Ammon, C.J., Herrmann, R.B. & Correig, A.M., 2000. Joint inversion of receiver function and surface wave dispersion observations, *Geophys. J. Int.,* **143**(1), 99–112.

Kennett, B.L.N., 1991. The removal of free surface interactions from three-component seismograms, *Geophys. J. Int.,* **104**(1), 153–163.

Kim, S., Dettmer, J., Rhie, J. & Tkalčić, H., 2016. Highly efficient Bayesian joint inversion for receiver-based data and its application to lithospheric structure beneath the southern Korean Peninsula, *Geophys. J. Int.,* **206**(1), 328–344.

Kind, R., Ni, J., Zhao, W., Wu, J., Yuan, X., Zhao, L. & Hearn, T., 1996. Evidence from earthquake data for a partially molten crustal layer in southern Tibet, *Science,* **274**(5293), 1692–1694.

Kolb, J.M. & Lekić, V., 2014. Receiver function deconvolution using transdimensional hierarchical Bayesian inference, *Geophys. J. Int.,* **197**(3), 1719–1735.

Kosarev, G.L., Petersen, N.V., Vinnik, L.P. & Roecker, S.W., 1993. Receiver functions for the Tien Shan analog broadband network: contrasts in the evolution of structures across the Talasso-Fergana fault, *J. geophys. Res.: Solid Earth,* **98**(B3), 4437–4448.

Kumar, M.R. & Bostock, M.G., 2008. Extraction of absolute P velocity from receiver functions, *Geophys. J. Int.,* **175**(2), 515–519.

Langston, C.A. & Liang, C., 2008. Gradiometry for polarized seismic waves, *J. geophys. Res.: Solid Earth,* **113**(B8).

Ledoit, O. & Wolf, M., 2004. A well-conditioned estimator for large-dimensional covariance matrices, *J. Multivariate Anal.,* **88**(2), 365–411.

Ligorria, J.P. & Ammon, C.J., 1999. Iterative deconvolution and receiver-function estimation, *Bull. seism. Soc. Am.,* **89**(5), 1395–1400.

Li, J., Song, X., Zhu, L. & Deng, Y., 2017. Joint inversion of surface wave dispersions and receiver functions with P velocity constraints: application to Southeastern Tibet, *J. geophys. Res.: Solid Earth,* **122,** 7291–7310.

Li, M., Zhang, S., Bodin, T., Lin, X. & Wu, T., 2018. Transdimensional inversion of scattered body waves for 1D S-wave velocity structure—application to the Tengchong volcanic area, Southwestern China, *J. Asian Earth Sci.,* **159,** 60–68.

Li, X. *et al.*, 2003. Receiver function study of the Hellenic subduction zone: imaging crustal thickness variations and the oceanic Moho of the descending African lithosphere, Geophys, *J. Int.,* **155**(2), 733–748.

Malinverno, A., 2000. A Bayesian criterion for simplicity in inverse problem parametrization, *Geophys. J. Int.,* **140**(2), 267–285.

Malinverno, A., 2002. Parsimonious Bayesian Markov chain Monte Carlo inversion in a nonlinear geophysical problem, *Geophys. J. Int.,* **151**(3), 675–688.

Marshak, S., Domrois, S., Abert, C., Larson, T., Pavlis, G., Hamburger, M. & Chen, C., 2017. The basement revealed: tectonic insight from a digital elevation model of the Great Unconformity, USA cratonic platform, *Geology,* **45**(5), 391–394.

Mooney, W.D.(2015), Crust and lithospheric structure—global crustal structure, in *Treatise of Geophysics,* 2nd edn, Vol. **1,** pp. 339–390, Elsevier.

Nelson, K.D., Baird, D.J., Walters, J.J., Hauck, M., Brown, L.D., Oliver, J.E. & Sloss, L.L., 1993. Trans-Hudson orogen and Williston basin in Montana and North Dakota: new COCORP deep-profiling results, *Geology,* **21**(5), 447–450.

Olugboji, T.M., Lekic, V. & McDonough, W., 2017. A statistical assessment of seismic models of the US continental crust using Bayesian inversion of ambient noise surface wave dispersion data, *Tectonics,* **36**(7), 1232–1253.

Owens, T.J., Zandt, G. & Taylor, S.R., 1984. Seismic evidence for an ancient rift beneath the Cumberland Plateau, Tennessee: a detailed analysis of broadband teleseismic P waveforms, *J. geophys. Res.: Solid Earth,* **89**(B9), 7783–7795.

Piana Agostinetti, N. & Malinverno, A., 2010. Receiver function inversion by trans-dimensional Monte Carlo sampling, *Geophys. J. Int.,* **181**(2), 858–872.

Reading, A., Kennett, B. & Sambridge, M., 2003. Improved inversion for seismic structure using transformed, S-wavevector receiver functions: removing the effect of the free surface, *Geophys. Res. Lett.,* **30**(19).

Rudnick, R.L. & Fountain, D.M., 1995. Nature and composition of the continental crust: a lower crustal perspective, *Rev. Geophys.,* **33**(3), 267–309.

Rychert, C.A. & Harmon, N., 2016. Stacked P-to-S and S-to-P receiver functions determination of crustal thickness, Vp, and Vs: the H-V stacking method, *Geophys. Res. Lett.,* **43**(4), 1487–1494.

Shapiro, N.M., Campillo, M., Stehly, L. & Ritzwoller, M.H., 2005. High-resolution surface-wave tomography from ambient seismic noise, *Science,* **307**(5715), 1615–1618.

Shen, W. & Ritzwoller, M.H., 2016. Crustal and uppermost mantle structure beneath the United States, *J. geophys. Res.: Solid Earth,* **121**(6), 4306–4342.

Shen, W., Ritzwoller, M.H. & Schulte-Pelkum, V., 2013. A 3-D model of the crust and uppermost mantle beneath the Central and Western US by joint inversion of receiver functions and surface wave dispersion, *J. geophys. Res.: Solid Earth,* **118**(1), 262–276.

Sivia, D. & Skilling, J., 2006. *Data Analysis: A Bayesian Tutorial*. OUP Oxford.

Tkalčić, H., Pasyanos, M.E., Rodgers, A.J., Gök, R., Walter, W.R. & Al-Amri, A., 2006. A multistep approach for joint modeling of surface wave dispersion and teleseismic receiver functions: implications for lithospheric structure of the Arabian Peninsula, *J. geophys. Res.: Solid Earth,* **111**(B11).

Ward, K.M., Zandt, G., Beck, S.L., Christensen, D.H. & McFarlin, H., 2014. Seismic imaging of the magmatic underpinnings beneath the Altiplano-Puna volcanic complex from the joint inversion of surface wave dispersion and receiver functions, *Earth planet. Sci. Lett.,* **404,** 43–53.

Whitmeyer, S.J. & Karlstrom, K.E., 2007. Tectonic model for the Proterozoic growth of North America., *Geosphere,* **3,** (4), 220–259.

Yeck, W.L., Sheehan, A.F. & Schulte-Pelkum, V., 2013. Sequential H-κ stacking to obtain accurate crustal thicknesses beneath sedimentary basins, *Bull. seism. Soc. Am.,* **103**(3), 2142–2150.

Yu, Y., Song, J., Liu, K.H. & Gao, S.S., 2015. Determining crustal structure beneath seismic stations overlying a low-velocity sedimentary layer using receiver functions, *J. geophys. Res.: Solid Earth,* **120**(5), 3208–3218.

Zelt, B.C. & Ellis, R.M., 1999. Receiver-function studies in the Trans-Hudson orogen, Saskatchewan, *Can. J. Earth Sci.,* **36**(4), 585–603.

Zhang, H., Lee, S., Wolin, E., Bollmann, T.A., Revenaugh, J., Wiens, D.A. & Stein, S., 2016. Distinct crustal structure of the North American Midcontinent Rift from P wave receiver functions, *J. geophys. Res.: Solid Earth,* **121**(11), 8136–8153.

Zorin, Y.A., Mordvinova, V.V., Turutanov, E.K., Belichenko, B.G., Artemyev, A.A., Kosarev, G.L. & Gao, S.S., 2002. Low seismic velocity layers in the Earth's crust beneath Eastern Siberia (Russia) and Central Mongolia: receiver function data and their possible geological implication, *Tectonophysics,* **359**(3–4), 307–327.

Özalaybey, S., Savage, M.K., Sheehan, A.F., Louie, J.N. & Brune, J.N., 1997. Shear-wave velocity structure in the northern Basin and Range province from the combined analysis of receiver functions and surface waves, *Bull. seism. Soc. Am.,* **87**(1), 183–199.

SUPPORTING INFORMATION

Supplementary data are available at *GJI* online.

Figure S1. Individual receiver functions at station C25A sorted by the backazimuth (left panel, top right panel for zoomed-in view between 300° and 321°). Bottom right-hand panel shows the average RF at different bins based on their ray parameters. Individual RFs are coloured based on their bin number in the left- and top right-hand panel using the same colour scheme as bottom right-hand panel.

Downloaded from https://academic.oup.com/gji/article-abstract/219/2/1032/5539534 by University of Maryland user on 03 September 2019

Figure S2. Same as Fig. S1, but for C31A.
Figure S3. Same as Fig.S3, but for C35A.
Figure S4. Left panel: V_s depth distributions retrieved using transdimensional Bayesian inversion of SWD and Ps RF data from station C25A-TA (right: red). The ensemble solutions are displayed as probability density functions at each depth, with warmer colours corresponding to higher posterior probabilities, and the solid red line denoting the 5 per cent trimmed mean of the posterior. Middle panel: transition probability of the V_s ensemble calculated at every kilometre. Note that the transition probability only takes into account the occurrences of the velocity change, not the change of value associated with them. Therefore, large amplitude velocity changes that have a low probability show up as simply low probability ones in the transition probability plots. Conversely, high probability but low amplitude velocity changes show up as high probabilities of transition. Right panel: from top to bottom-hand: Rayleigh wave dispersion, Love wave dispersion, and original Ps receiver function data fit. Data are denoted in red while values predicted by the ensemble solution are plotted as probability density functions. The inversion scheme is described in the detailed method description section in the supporting information.
Figure S5. Same as Fig. S4, but for station C31A-TA.
Figure S6. Same as Fig. S4, but for station C35A-TA.
Figure S7. Left panel: V_s depth distributions at the top 15 km retrieved using transdimensional Bayesian inversion of surface wave dispersion and Ps receiver function data. The ensemble solutions are displayed as probability density functions at each depth, with warmer colours corresponding to higher posterior probabilities, and the solid red line denoting the 5 per cent trimmed mean of the posterior. Right-hand panel: transition probability of the V_s ensemble calculated at every 100 m.
Figure S8. Same as Fig. S4, except that the resonance removal filter has been applied to Ps receiver function for C25A-TA.
Figure S9. Same as Fig. S5, but SWD in the 15–40 s range is used here instead of the 5–40 s period range used elsewhere.
Figure S10. Left-hand panel: V_s depth distributions retrieved using transdimensional Bayesian inversion of surface wave dispersion data from station C31A-TA. The ensemble solutions are displayed as probability density functions at each depth, with warmer colours corresponding to higher posterior probabilities, and the solid red line denoting the 5 per cent trimmed mean of the posterior. Right-hand panel: Rayleigh (top) and Love (bottom) wave dispersion data fit. Data are denoted in red colour; while values predicted by the ensemble solution are plotted as probability density functions.
Figure S11. Left panel: V_s depth distributions retrieved using transdimensional Bayesian inversion of Ps RF data from station C31A-TA (right: red). The ensemble solutions are displayed as probability density functions at each depth, with warmer colours corresponding to higher posterior probabilities, and the solid red line denoting the 5 per cent trimmed mean of the posterior. Right-hand panel: original Ps receiver function data fit. Data are denoted in red while values predicted by the ensemble solution are plotted as probability density functions.
Figure S12. Left panel: V_s depth distributions retrieved using transdimensional Bayesian inversion of synthetic surface wave dispersion and Ps receiver function data. The ensemble solutions are displayed as probability density functions at each depth, with warmer colours corresponding to higher posterior probabilities, and the solid red line denoting the 5 per cent trimmed mean of the posterior. The target model (black dashed lines) is used to generate synthetic data. Right-hand panel: transition probability of the V ensemble calculated at every kilometre.
Figure S13. Same as Fig. S10, but for C25A-TA.
Figure S14. Posterior of transdimensional Bayesian inversion of surface wave dispersion and sediment-corrected receiver functions for synthetic model (shown in black dashed line). The ensemble solutions are displayed as probability density functions at each depth, with warmer colours corresponding to higher posterior probabilities, and the solid red line denoting the 5 per cent trimmed mean of the posterior. Right-hand panel: From top to bottom: Rayleigh wave dispersion, Love wave dispersion, and original Ps receiver function data fit. Data are denoted in red while values predicted by the ensemble solution are plotted as probability density functions.
Table S1. Assumed free-surface velocities for stations C25A, C31A and C35A.

Please note: Oxford University Press is not responsible for the content or functionality of any supporting materials supplied by the authors. Any queries (other than missing material) should be directed to the corresponding author for the paper.

Downloaded from https://academic.oup.com/gji/article-abstract/219/2/1032/5539534 by University of Maryland user on 03 September 2019